Metallurgical Characterization of SS 316L Repurposed by Wire Plus Arc Additive Manufacturing

Duong Vu[1], Van Thao Le[2,*]

[1]School of Engineering Technology, Duy Tan University, Da Nang, Vietnam

[2]ATC, Le Quy Don Technical University, Hanoi, Vietnam

Received 17 January 2023; received in revised form 14 February 2023; accepted 21 February 2023

DOI: https://doi.org/10.46604/ijeti.2023.11417

Abstract

This research aims to analyze the microstructures and mechanical characteristics of stainless steel (SS) 316L repurposed by wire plus arc additive manufacturing (WAAM). The SS 316L wire is deposited on a SS 316 substrate, which can be repurposed. This deposited material underwent optical microscopy, X-ray diffraction, and tensile test, and the results indicate that it features cellular and columnar dendrites at the bottom and equiaxial grains at the top. The tensile strength of the interface region between the deposited material (DM) and the base material (BM) is the highest (559 ± 4.16 MPa vs. 510 ± 4.93 MPa in DM and 540 ± 2.65 in BM), indicating that the BM and the deposited layers are strongly bonded. All the results from the defect observation, microstructures, and mechanical characteristics confirm the potential of the WAAM process for repurposing.

Keywords: wire plus arc additive manufacturing, repurposing, 316L, metallurgical characterization

1. Introduction

In recent decades, directed energy deposition (DED) – a category of metal additive manufacturing (AM) technologies is widely investigated to produce medium to wide-size components in marine, aeronautic, molds, and dies [1]. The DED technologies can be classified into powder-feeding and wire-feeding DED processes. The powder-feeding DED processes generally use a laser energy source to melt the metal powder. The wire-feeding DED processes, known as wire plus arc additive manufacturing (WAAM), use an electric arc source to melt metal wire [2]. Most of the available advanced repairing techniques adopt powder-feeding DED processes [3]. However, the powder-feeding DED processes reveal a low deposition efficiency and high production costs. It is worth mentioning that the use of metallic wires in WAAM enables enhancing the deposition efficiency and the deposition rate and reducing harmful impacts to operators and the environment. Compared to traditional repairing processes (e.g., tungsten arc welding, brazing, and metal spaying) [4], WAAM can automatically add complex shapes and large regions [5-6].

Several authors have investigated the WAAM process for repairing components. For example, Li et al. [7] proposed a process planning for repairing the surface defect of metallic components based on the combination of machining and WAAM processes. Lee et al. [8] adopted the WAAM technique to repair damaged gray-casting iron parts of machine tools (e.g., the cross slide of a lathe). Hong et al. [6] remanufactured the large hot-forging die utilizing the WAAM process. The authors proposed two remanufacturing strategies - normal AM and vertical AM. The vertical AM strategy consisted of discretizing the model into the layers along the vertical direction, while in the normal AM strategy, the multi-layer model

* Corresponding author. E-mail address: vtle@lqdtu.edu.vn

English language proofreader: Hsin-Te Hsieh

was constructed by the normal offsetting algorithm [6]. Priarone et al. [9] recently repaired H13-steel mold inserts using the WAAM and computer numerical control (CNC) machining processes. The authors showed that the WAAM + CNC machining repairing approach allowed the materials and energy consumption savings.

Although there was a lot of research about repairing and remanufacturing damaged components with the WAAM technologies combined with CNC machining, very few research works were concentrated on the microstructures and performance of the deposited material (DM), the base metal (BM), and the metallurgical bonding in the interface between DM and BM for the repurposing applications. Practically, the BM and DM will work together. Therefore, it is not sufficient to investigate only the DM. The bonding between the base metal and the deposited layer is essential [10].

316L steel is largely employed in aeronautics and other industries because of its superior corrosion resistance and weldability. The WAAM process of 316L steel is widely investigated in previous studies [11]. However, the repurposing of 316L steel components by the WAAM process has not been reported yet. In the repurposing process, the material of the damaged part is directly reused to produce a new part with new features and functionalities without the need for a material recycling stage [12-13] (Fig. 1). The repurposing is different from the repairing process, as shown in Fig. 1. The repairing strategy simply recovers damaged regions of the part to the original shape to extend the part's life. The quality and warranty of the repaired part are generally less than the newly fabricated one [14]. On the other hand, the repurposing strategy aims to transform a used part into a new part with new geometry and functionality for new applications [15].

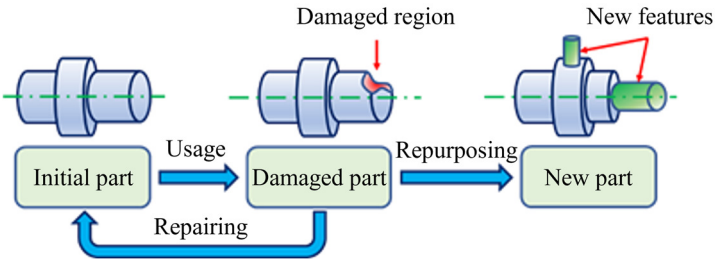

Fig. 1 Schema of the repurposing and repairing of damaged parts

Depending on the status and damage level of the used part, the repairing, repurposing, and material recycling strategies will be selected. If the damaged part cannot be repaired, repurposing will be considered to reuse the valuable material part of the damaged part. In other cases, the material recycling strategy is used to transform the damaged part into ingots. Compared to the recycling strategy, repurposing can conserve energy previously consumed to make the used part. By adding only the necessary features to the existing core to obtain the target part, energy consumption and production costs are reduced through the repurposing strategy [9, 13].

To obtain the target part, three main stages were applied, namely (i) the preparation of the repurposed region, (ii) the deposition of the material into the prepared region to recover the initial part shape or add new features, and (iii) the post-processing by machining and heat treatments [3]. The stress relieving methods can also be used to remove residual stress presented in the repurposed component after the WAAM deposition [15]. In the repurposing, the material performance (i.e., microstructures and mechanical properties), and the metallurgy bonding strength between the BM and DM directly influence the lifespan of the repurposed part. Therefore, the current study aims at validating the material performance of the 316L steel samples repurposed by the WAAM process.

2. Materials and Methods

In this section, the materials and methods used in the experiments were described. The samples were fabricated by depositing new features on the plates, which were considered as the used parts to be repurposed. To analyze the microstructures of the entire sample, the optical microscope (OM) and other characterization techniques, such as X-ray diffraction (XRD), and

scanning electron microscope (SEM) with energy dispersive spectroscopy (EDS) were utilized. The mechanical characteristics (e.g., microhardness and tensile properties) were also tested.

2.1. Materials

Fig. 2(a) presents the gas metal arc welding (GMAW)-WAAM system. The system is composed of a GMAW source, wire and shielding gas feeders, and a 6-axis Panasonic robot (TA1400). The 316L steel welding wire with a diameter of 1.2 mm supplied by Kiswel was used as the feedstock material in the GMAW-WAAM process. The chemical composition of the wire is composed of 11.16% Ni, 18.14% Cr, 2.23% Mo, 1.74% Mn, 0.40% Si, 0.02% C, and the balance percentage of Fe (in wt.%). The specification of the filler wire spool established by American Welding Society (AWS) is A5.9 ER316L. The 316 steel plate with dimensions of 80 × 200 × 20 mm (in width × length × height) was considered as a component to be repurposed. The plate's chemical composition includes (16~18%) Cr, (10~14%) Ni, (≤ 3.0%) Mo, (≤ 2.0%) Mn, (≤ 0.75%) Si, (≤ 0.03%) C, and the balance percentage of Fe (in wt.%).

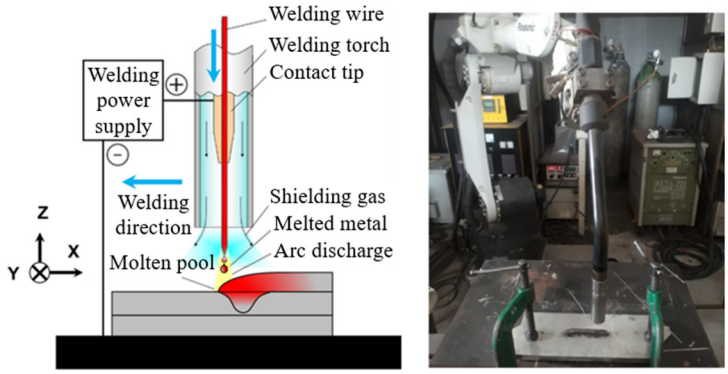

(a) The WAAM system

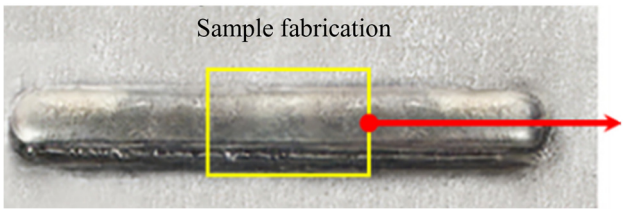

(b) The deposited sample

(c) The specimen for analyzing porosity, microstructure, and microhardness

Fig. 2 The WAAM system and fabrication of the sample

2.2. Metallurgical and microhardness tests

A single-bead wall with five layers, 60 mm in length, and 10 mm in height was built on the reused substrate by the GMAW-WAAM process (Fig. 2(b)) according to the zig-zag deposition strategy. The average layer height is about 2 mm. Before the deposition, the plate surface was ground and cleaned to remove the oxide layer and contamination layer. In this study, it is supposed that the deposited wall is the new feature built on the existing part (i.e., the substrate). The variables employed for the sample fabrication are described in Table 1. During the deposition, argon gas with a flow rate of 15 L/min was used for the shielding, and the mode of spray transfer was utilized. The speed of wire feeding is controlled by the GMAW system automatically based on the current value. The delay time between two successive deposited layers is 40 s and the workpiece was cooled down naturally at room conditions.

Table 1 The parameters used for the fabrication of the sample

Parameters	Current I (A)	Voltage U (V)	Deposition speed v (m/min)	Flow rate of the shielding gas (L/min)	Delay time between adjacent layers (s)
Value	110	22	0.3	15	40

A specimen (Fig. 2(c)) was extracted from the deposited metal and the base metal in the middle zone with a length of 30 mm (Fig. 2(b)). To analyze the metallurgical characterization of the DM and substrate material, this specimen was cleaned, ground with silicon carbide papers, and polished with a diamond-polishing agent of 2.5-µm particles. Finally, it was etched with a solution of 20 ml hydrochloric acid (HCl), 10 ml nitric acid (HNO3), and 20 ml glycerol for one minute. The microstructures were observed by an OM (A2M AXIO imager, Carl Zeiss). The chemical composition and microstructures were analyzed with the EDS technique integrated with a SEM (model SU3500). The phase analysis of the deposited and substrate materials was performed on a high-resolution X-Ray diffractometer (ARL EQUINOX 5000 series). The X-ray computed tomography (CT) technique was employed to assess the porosity. The microhardness was also tested by a hardness tester (Duramin-2, Struers). Each test was performed with a load of 980.70 mN and a dwell time of 10 s.

2.3. *Tensile tests*

For the tensile tests, another deposition of ten layers on another substrate was performed (Fig. 3(a)). The tensile specimens were cut horizontally with a wire cut EDM machine at three regions, including the DM, the interface region, and the base/substrate material (BM) (Fig. 3(b)), using. In each region, the three specimens with the same dimensions (Fig. 3(c)) were prepared. All the tensile specimens were designed according to ASTM E8M-13a standard. The tensile tests were carried out on a tensile machine. The tensile velocity was 12 mm/min. The broken surfaces of the samples after the tensile tests (Fig. 3(d)) were observed by the SEM technique.

(a) The deposited sample

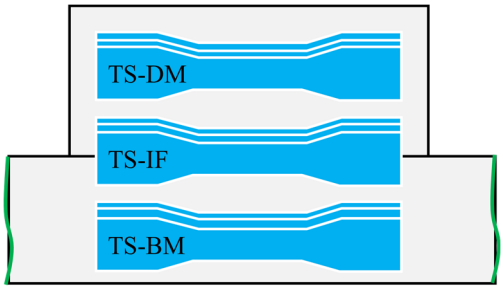

(b) Illustration of the tensile specimens and their locations

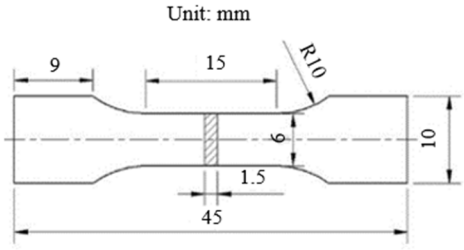

(c) The dimensions of tensile specimens

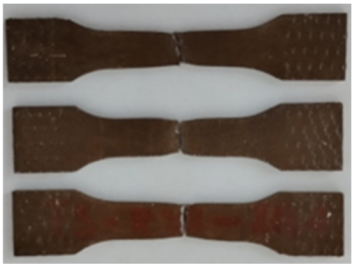

(d) The tensile specimens fractured after the tests

Fig. 3 Fabrication of tensile specimens

2.4. *Thermal simulation*

To interpret the relationship between the microstructure evolution and the thermal phenomenon during the deposition process, the finite element (FE) method has been utilized to observe the thermal evolution in the deposited layers. The ANSYS software was utilized to simulate the thermal evolution during the deposition process. In this article, the model based on the first law of thermodynamics (energy conservation) and the solution of the solid multiphase transient heat conduction equation for a moving heat source was used to simulate the temperature evolution during the WAAM process. The temperature evolution is governed by

$$\frac{\partial}{\partial x}\left(K\frac{\partial T}{\partial x}\right)+\frac{\partial}{\partial y}\left(K\frac{\partial T}{\partial y}\right)+\frac{\partial}{\partial z}\left(K\frac{\partial T}{\partial z}\right)+\dot{Q}=\rho C_p\left(\frac{\partial T}{\partial t}-v\frac{\partial T}{\partial x}\right) \quad (1)$$

where K is the thermal conductivity, T is the temperature, Cp is the specific heat, ρ is the material density, v is the speed of the heat source, and $\dot{\boldsymbol{Q}}$ is the volume heat source [16].

The initial temperature (denoted by T_{ini}) of the testing environment and the substrate are equal to 25 °C. The boundary conditions of convection and radiation on the surfaces are described by

$$-\left\langle \frac{\partial T}{\partial x}, \frac{\partial T}{\partial y}, \frac{\partial T}{\partial z} \right\rangle \cdot \vec{n} = \varepsilon\sigma\left(T^4 - T_{ini}^4\right) + h\left(T - T_{ini}\right) \tag{2}$$

where σ is the Stefan-Boltzmann constant, σ = 5.67 × 10^{-8} W.m^{-2}.K^{-4} [17]; $\vec{\boldsymbol{n}}$ depicts the unitary normal vector of the surfaces; ε is the emissivity coefficients of the sample surfaces, ε = 0.9 [18]; h is the local heating exchange coefficient, h = 30 W.m^{-2}.K^{-1} [18]. Moreover, we also used h = 400 W.m^{-2}.K^{-1} for the substrate surface that contacts the building table [16].

For the deposition process, the approach of element activation and deactivation Goldak's model of the arc source described in previous studies have been applied. The geometrical model was constructed using the average dimensions of the deposited layers (i.e., the average value of layer width, deposition length, and layer height) and the substrate's dimensions. The mesh model was built with linear-brick-eight-node elements. To assure the prediction accuracy and reduce the computation time, the mesh of the substrate is coarser than the mesh of the deposited layer and the region of the substrate surrounding the deposited layer (Fig. 4). Bui et al. [19] has detailed the simulation model. The thermal evolution cycles were extracted at the center point of each deposited layer, as shown in Fig. 4(a). The simulation result on thermal evolution and distribution during the deposition is shown in Fig. 4(b).

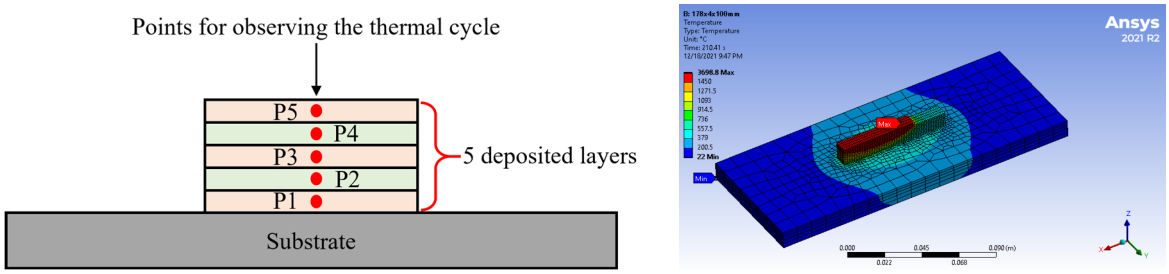

(a) Positions for observing the thermal cycle (b) Thermal evolution and distribution

Fig. 4 Thermal cycle analysis via the FE simulation

3. Experimental Results and Discussion

In this section, the microstructures of the BM, heat-affected zone (HAZ), and DM were deeply analyzed. The mechanical characteristics (e.g., microhardness and tensile properties) were also discussed. Once the material performance of the entire part is confirmed through this investigation, the repurposing process using the WAAM technology is applied to specific components.

3.1. Macro analysis

Fig. 5(a) reveals that there are no cracks and lack of fusion between deposited layers and the substrate. There is only a very small pore with a volume of 0.02 mm^3 and a boundary diameter of 0.42 mm appearing in the deposited layer (Fig. 5(b)). This confirms a good quality and bonding of deposition. The density in the substrate is also good with only three very small pores, which present a volume inferior to 0.03 mm^3 (Fig. 5(b)). The depth of penetration of the deposited layer into the substrate is about 1.8 mm (Fig. 5(a)). The X-ray testing image of the whole deposited sample indicated that there was also no lack of fusion between the substrate and the deposited metal for the whole deposited sample (Fig. 5(c)). Indeed, if there are major defects, the deposited region will have black or gray patches in the X-ray image. The microstructural images captured in different locations in the DM and BM (Fig. 6) again confirm a great bonding between the layers and between the DM and BM.

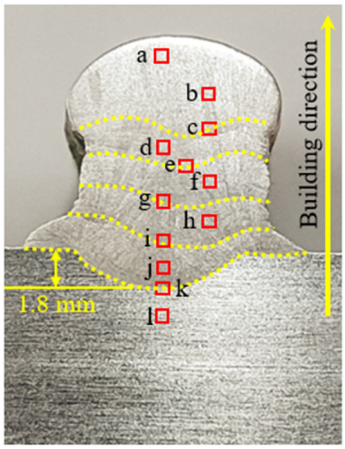

(a) Macrostructure

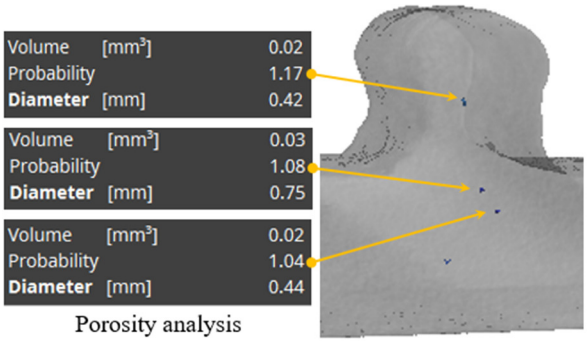

(b) The porosity analysis by X-ray CT

(c) The lack of fusion verified by the X-ray machine testing

Fig. 5 Results on the porosity and lack of fusion analysis

3.2. Microstructure observation

Fig. 6 shows the images captured by the OM in different zones from the top of the deposited feature to the substrate (Fig. 5(a)). The microstructures in both the added material and the substrate mainly consist of γ-austenite and δ-ferrite phases. The γ-austenite phase is dominant while only a little amount of δ-ferrite phases remained in the boundaries of γ-austenite grains, as presented in Fig. 6(a) to Fig. 6(d).

The δ-ferrite phases exist in vermicular, skeletal, and lathy morphologies, depending on the cooling rates. For example, when the cooling rates are moderate, δ-ferrite exists in the form of vermicular or skeletal morphologies. On the other hand, when the cooling rates are high, the lathy morphology of δ-ferrite is formed. For 316L stainless steel (SS), δ-ferrite phase is a body-centered cubic (BCC) structure, which is relatively soft, ductile, and easily machinable, whereas γ-austenite phase is a face-centered cubic (FCC) structure, which is relatively hard, brittle, and strong.

For the deposited layers, in general, the lower layers feature finer grains as compared to the higher layers. As shown in Fig. 6, the width of columnar grains of the first layer (Fig. 6(j)) is the narrowest, followed by the 2nd layer (Fig. 6(h)), the 3rd layer (Fig. 6(f)), the 4th layer (Fig. 6(d)) and the 5th layer (Fig. 6(b)), respectively. The average width of the columnar grains of the first to the fifth layer is 4.16 ± 0.66 μm, 6.35 ± 0.80 μm, 8.98 ± 1.20 μm, 9.31 ± 0.75 μm, and 9.45 ± 1.24 μm, respectively.

This phenomenon can be explained by heat accumulation, cooling rate, and thermal gradient [20]. Because of the cold substrate capacity or thermal dissipation, the cooling rate is the highest in the first layer. As the deposited layers augment, the heat accumulation and the interlayer temperature after 40 s of natural cooling increase, resulting in longer cooling times and lower cooling rates [21]. As shown in Fig. 7, the first temperature peak of the thermal cycle gradually increments from the first layer (3196 ℃) to the fifth layer (3670 ℃).

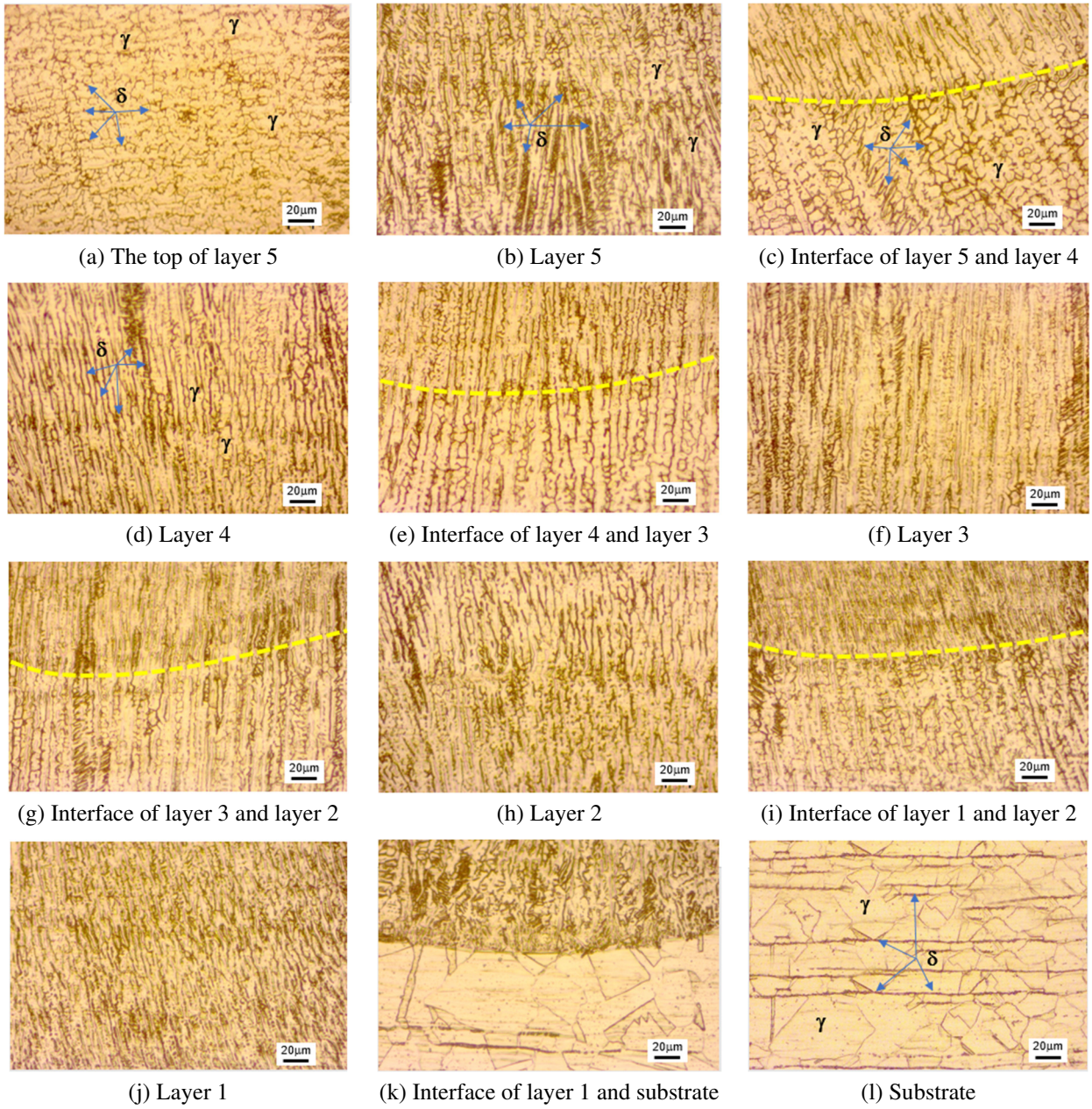

(a) The top of layer 5 (b) Layer 5 (c) Interface of layer 5 and layer 4

(d) Layer 4 (e) Interface of layer 4 and layer 3 (f) Layer 3

(g) Interface of layer 3 and layer 2 (h) Layer 2 (i) Interface of layer 1 and layer 2

(j) Layer 1 (k) Interface of layer 1 and substrate (l) Substrate

Fig. 6 Microstructures in different areas from (a) to (l) of the whole sample (Fig. 4(a))

Similarly, the interlayer temperature of the deposited layer after 40 s of the natural cooling increases from the first layer (420 ℃) to the fifth layer (780 ℃). This indicates the heat accumulation during the deposition. This phenomenon return causes a decrease in the cooling rate from the first layer (169 ℃/s) to the fifth layer (142 ℃/s). According to the following relationship between the grain size and the cooling rate: $\lambda = 50 \bullet r^{-0.4}$ [22], where λ (μm) is the width of columnar grains and r (K/s) is the cooling rate, the grain size decreases with the increase in the cooling rate. As a result, the first layer shows the finest grains, followed by the second layer to the fifth layer, as previously mentioned.

Moreover, due to the reheating effect of the subsequent layer on the previous layer, the top region of the first to the fourth layers reveals coarser grains (Fig. 6(i), Fig. 6(g), Fig. 6(e), and Fig. 6(c)). For instance, in the second layer, the average size of grains in the bottom region is 6.35 ± 0.80 μm, while that value in the top region is 8.11 ± 1.50 μm. In the third layer, the average grain size is 8.98 ± 1.20 μm (in the bottom region) and 11.59 ± 1.20 μm (in the top region). This phenomenon is consistent with those reported in previous studies. On the other hand, the top of the last deposit (i.e., the fifth layer) shows equiaxed grains with an average grain size of 14.23 ± 0.9 μm (Fig. 6(a)). This is because the top of this layer was not affected by the reheating and remelting processes of other layers. The growth rate and thermal gradient were also the lowest.

In a layer – for example, the third layer (Fig. 6(g), Fig. 6(f), and Fig. 6(e)), the microstructure reveals cellular grains in the bottom region close to the fusion line (Fig. 6(g)). Thereafter, cellular grains were transformed into narrow columnar dendrites (Fig. 6(f)), which gradually enlarged towards the top area. Due to the reheating and remelting effects of the fourth layer, the grains were finally transformed into secondary equiaxed dendrites (Fig. 4(e)).

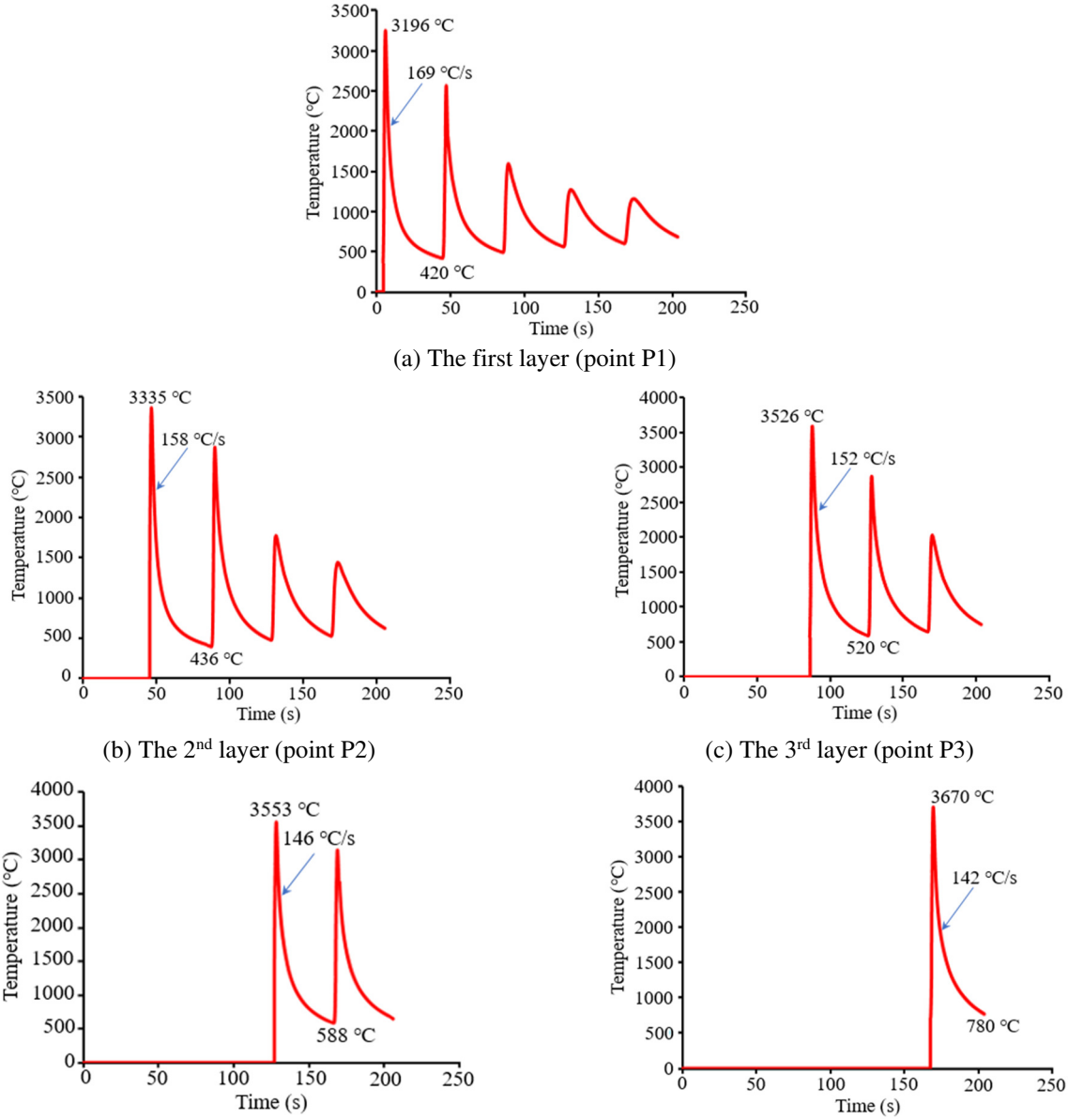

(a) The first layer (point P1)

(b) The 2nd layer (point P2)

(c) The 3rd layer (point P3)

(d) The 4th layer (point P4)

(e) The 5th layer (point P5)

Fig. 7 The thermal evolution cycles at the middle points of different layers (the points P1 to P5 indicated in Fig. 4(a))

According to the SEM-EDS analysis results (Fig. 8 and Table 2), it is revealed that the percentage in weight of chemical elements (e.g., Cr, Ni, Mn, Mo, and Si) in different deposited layers is nearly homogenous. It is worth noting that the EDS technique is limited to detecting the element with a weight percentage inferior to 0.1% [23]. Therefore, the chemical components such as C, P, S, and Cu were not included in the analysis of the weight percentage. In all the five deposited layers, the ratio Cr_{eq}/Ni_{eq} falls in an interval between 1.48 and 1.95, where Cr_{eq} = %Cr + %Mo + 1.5•%Si + 0.5•%Nb and Ni_{eq} = %Ni + 30%•C + 0.5•%Mn. Accordingly, the microstructure development of the DM is with respect to the FA solidification mode [20, 24], as described by

$$L \rightarrow L + \delta\text{-ferrite} \rightarrow L + \delta\text{-ferrite} + \gamma\text{-austenite} \rightarrow \delta\text{-ferrite} + \gamma\text{-austenite} \quad (3)$$

where L is the liquid phase.

Table 2 SEM-EDS analysis results on the chemical composition in five deposited layers

Layer	Chemical composition (wt.%)								
	Cr	Ni	C	Mn	Mo	Si	Cr_{eq}	Ni_{eq}	Cr_{eq}/Ni_{eq}
Layer 1	18.04	9.43	0.00	3.68	2.05	0.47	20.80	11.27	1.85
Layer 2	17.76	9.84	0.00	3.05	2.04	0.61	20.72	11.37	1.82
Layer 3	17.54	9.52	0.00	3.68	2.46	0.49	20.74	11.36	1.83
Layer 4	17.62	9.24	0.00	3.60	2.11	0.59	20.62	11.04	1.87
Layer 5	15.53	7.96	0.00	3.61	1.72	0.41	17.87	9.77	1.83

This result again confirms, in theory, that the microstructures of the specimen are mainly composed of γ-austenite and δ-ferrite phases at room temperature, as observed in Fig. 6. The ferrite phases present in skeletal/vermicular and lathy forms, depending on the cooling rate [25]. As the cooling rate is moderate, ferrites exist in vermicular/skeletal morphologies, and they are in lathy forms when the cooling rate is elevated.

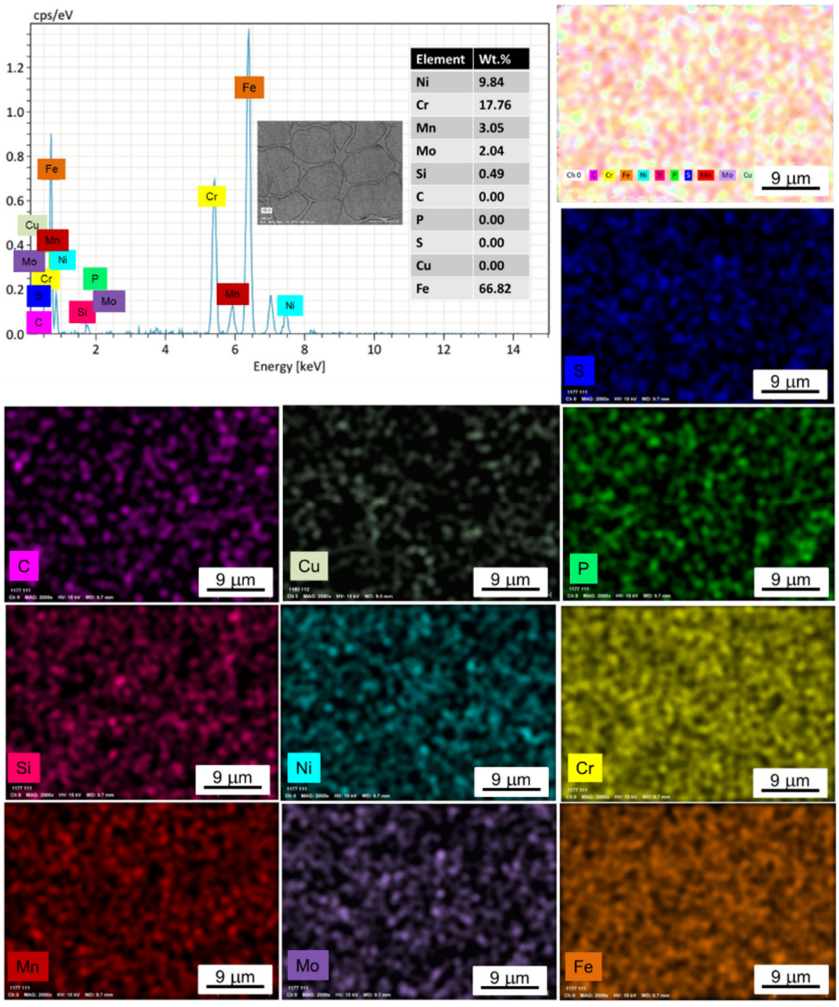

Fig. 8 EDX analysis results and the mapping of elements in the middle of the deposited feature

For the microstructure in the interface region, Fig. 6(k) and Fig. 9 present the microstructures in the interface area between the added material and the substrate. The interface line is nearly parabolic, and the microstructures close to the interface line are very fine. The austenite grains grow up and coarser in dendrite and skeletal forms in the middle area of penetration. The grain size in microstructures of the substrate material near the interface line (Fig. 6(k)) is coarser than that in the center of the substrate (Fig. 6(l)). This is mainly due to the heat input of the first layer. However, the heat-affected region (HAR) of the substrate is very narrow, about 114 µm in width (Fig. 9). In the HAR, the microstructures are mainly composed of equiaxed grains with larger size (with an average value of 48.54 ± 9.83 µm) compared to those in the substrate

region with an average grain size of 25.82 ± 7.54 μm. On the other hand, in the center of the substrate, the microstructures show equiaxed grains in bands of austenite, and ferrite is aligned along the rolling direction (Fig. 6(l)). From this observation, it can be concluded that the heat in the deposition process has less effect on the substrate.

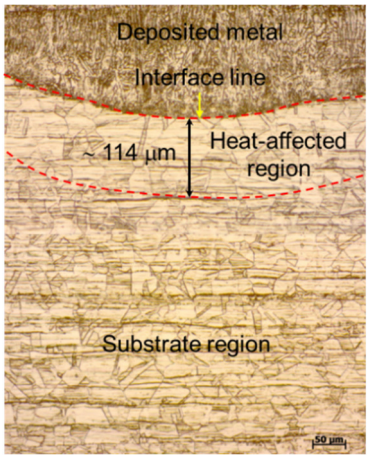

Fig. 9 Microstructures in the interface region

The phases observed in the OM analysis were also confirmed by the XRD results (Fig. 10). The diffraction graphs in both the added area and the substrate exhibit a dominant presence of austenite and weak traces of ferrite. The highest peak (1 1 1) indicates austenite matrices, whereas the small peak (1 1 0) corresponds to ferrite phases. The second strong peak (2 0 0) presents columnar austenite grains.

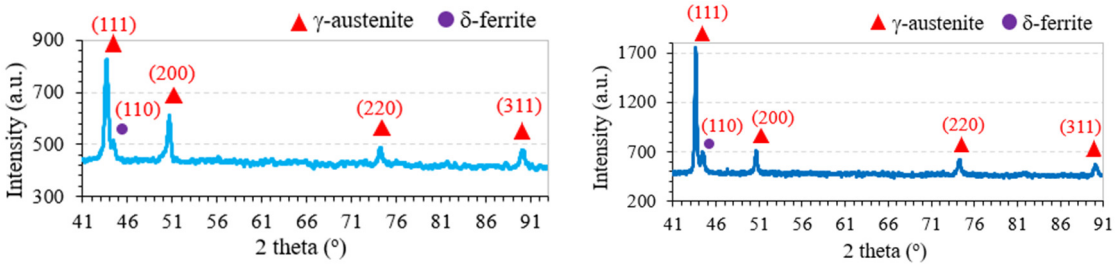

(a) The deposited material (b) The base material

Fig. 10 XRD analysis results

3.3. Microhardness

Fig. 11(a) describes the microhardness of the specimen. The average microhardness of the substrate is 184 HV0.1 with a small deviation of 1.53 HV0.1. Meanwhile, the microhardness shows a decreasing trend along the building direction. The average microhardness in the bottom (L1), the middle (i.e., L2 to L4), and the top (L5) of the deposited part are 193 ± 3.61, 168 ± 12.56, and 162 ± 4.93 HV0.1, respectively. Moreover, in a deposited layer, the microhardness generally decreases from the bottom to the top area. This result is consistent with the microstructure observed previously. According to the Hall-Petch behavior [26], the microhardness is strongly correlated with the grain size, which is shown as

$$HV = HV_0 + K_H \cdot d^{-\frac{1}{2}} \tag{4}$$

where K_H and HV_0 are the constants regarding the material and the hardness measurement, and d is the grain size.

In the deposited part, due to the reheating cycles and heat accumulation, the grains are coarse along the build direction and the layer height, as discussed previously. Hence, the average microhardness gradually decreases along the depositing direction. The high-cooling speed occurred in the first layer because it was directly deposited on the cold plate, resulting in the smallest grains in microstructures. Therefore, the highest average microhardness was observed in this layer. Moreover,

the microhardness measured along the interface line also falls in the range of microhardness measured in the DM (Fig. 11(b)). The microhardness in the penetration region (points P3 to P6) is higher than that measured at the points {P1, P2, P7, and P8} in the edge region of the first layer.

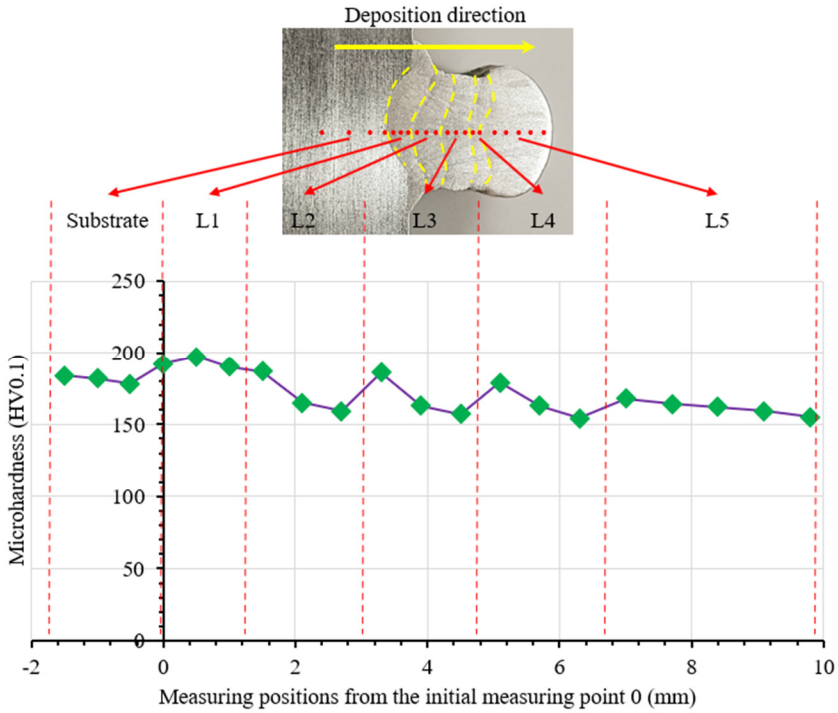

(a) Microhardness measured along the build direction

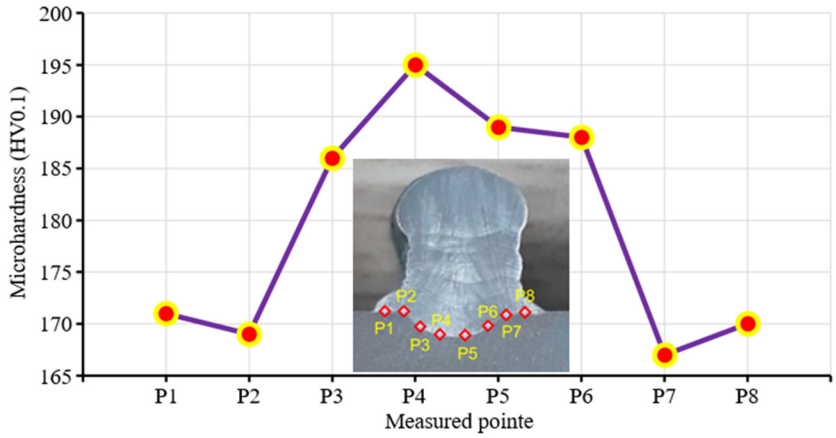

(b) Microhardness measured along the interface line

Fig. 11 Microstructures in the interface region

3.4. Tensile properties

Table 3 shows the summary of tensile test results, and Fig. 12 presents a comparison of the average value of tensile strengths between the tensile specimens. It is shown that the average yield strength 0.2% ($YS_{0.2\%}$) of the DM region was the highest (337 ± 5.57 MPa), followed by the BM (332 ± 3.06 MPa) and the IF region (330 ± 3.21), respectively. However, the difference in YS among different regions was not significant (inferior to 5%). On the other hand, the IF region shows the highest average ultimate tensile strength (UTS) (559 ± 4.16 MPa), followed by the BM region (540 ± 2.65 MPa) and the DM region (510 ± 4.93 MPa). The reason was that the TS-IF samples have a part in the bottom of the deposited layer with the finest grain size and a part of the HAR of the substrate and the fusion line in the middle. The UTS of the IF region was higher than that of the BM, showing that the deposition process could significantly enhance the tensile strength of the BM. It also confirmed that the BM and the deposited layers were strongly bonded, and the deposition process was reliable and stable.

Table 3 Tensile test results

Samples	$YS_{0.2\%}$ (MPa)	UTS (MPa)
TS-DM1	332	508
TS-DM2	343	516
TS-DM3	336	507
Average	337 ± 5.57	510 ± 4.93
TS-IF1	328	554
TS-IF2	334	562
TS-IF3	329	560
Average	330 ± 3.21	559 ± 4.16
TS-BM1	329	538
TS-BM2	335	543
TS-BM3	331	539
Average	332 ± 3.06	540 ± 2.65

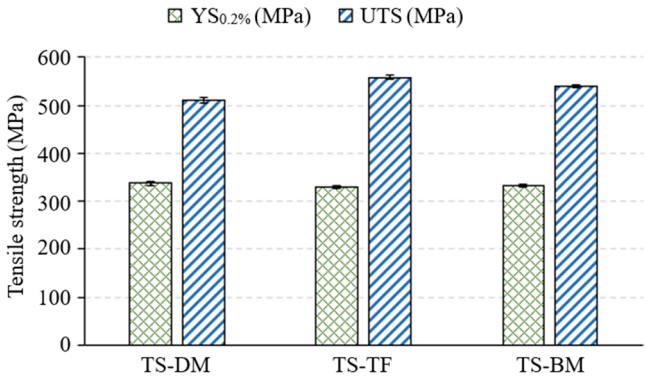

Fig. 12 Comparison of tensile strengths between the tensile specimens

Fig. 13 shows the fractured surface morphologies of the tensile samples in different regions. There were no major defects such as cracks and holes, indicating compact microstructures of the samples. The dimples observed on the fractured surfaces indicated the ductile fracture mechanism of all the samples. Due to the small grain size in the IF region, smaller and shallower dimples were observed on the fractured surface (Fig. 12(b)). On the other hand, the grain size is coarser in the DM, resulting in larger and deeper dimples on the fractured surface of the TS-DM samples.

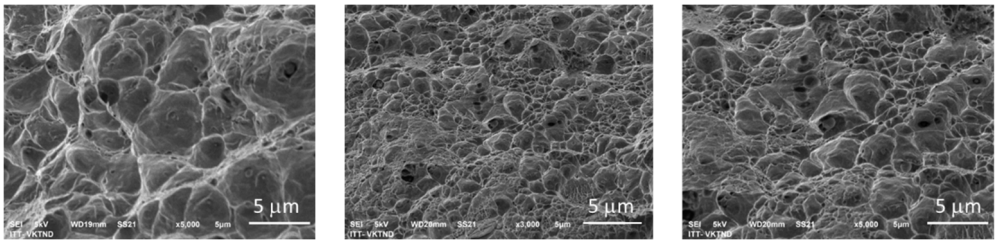

(a) TS-DM (b) TS-IF (c) TS-BM samples

Fig. 13 SEM images of the broken surfaces of the tensile specimen

All the results demonstrate the DM has strong bonding with the base material (BM), and they can work together as a unique part fabricated from a casting/wrought workpiece. Therefore, the repurposed part with its characteristics can be used in many applications as unique parts fabricated by conventional manufacturing pathways. Several cases reported in previous studies [27-28] (Fig. 14) can be considered as specific applications of the repurposing strategy. However, it should be noted that 316L is not suitable for applications at temperatures above 800 °C, as its mechanical properties start to degrade above this temperature. Moreover, SS 316L can be susceptible to pitting corrosion in environments with high chloride concentrations, such as seawater. Therefore, these limitations of SS 316L should be taken into consideration when selecting such material for various applications.

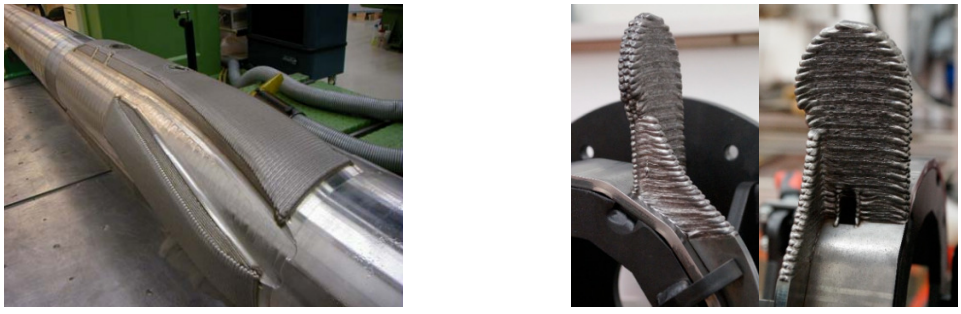

(a) The oil drilling tool with the "teeth" deposited by AM [27]

(b) The "exemplary part" obtained by depositing new features on the base part [28]

Fig. 14 Examples considered as repurposed parts for specific applications

4. Conclusions

This research explored the metallurgical characterization of SS 316L repurposed by the WAAM process. The microstructures of both the DM and the substrate material were analyzed. The microhardness and tensile properties of the repurposed component were also observed. Based on the obtained results, the conclusions of this study were drawn as follows:

(1) There are no cracks and major pores generated in the interface and deposited areas.

(2) The microstructures in both the added material and the substrate mainly consist of γ-austenite and δ-ferrite phases. The γ-austenite phase is dominant while only a small quantity of δ-ferrite phases remained in the boundaries of γ-austenite grains.

(3) Due to the complex of thermal cycles and temperature gradient in the deposited part, the DM reveals various grain morphologies, including fine columnar grains at the bottom and equiaxed dendrites at the top. This results in an uneven microhardness distribution from the bottom to the top layer.

(4) There is a continuous transition of microstructures between the DM and the substrate material, and the depth of penetration of the deposited layer into the substrate is about 1.8 mm, indicating a strong metallurgical bonding between the deposited feature and the substrate.

(5) The average microhardness of the DM ranged from 162 to 193 HV0.1, while the value of the base metal was about 184 HV0.1.

(6) The UTS of the IF region was the highest (559 ± 4.16 MPa vs. 510 ± 4.93 MPa in the DM region and 540 ± 2.65 in the BM region), again confirming that the BM and the deposited layers were strongly bonded.

(7) The HAR of the substrate is very narrow, demonstrating that the material properties in the core of the reused part are conserved.

The study confirms the feasibility of utilizing the WAAM process for repairing, remanufacturing, and repurposing applications. The repurposed parts made from SS 316L with their characteristics can be used for applications in which wear rate and corrosion behaviors are also crucial, for example, rolling shafts, cylinders, and boilers.

Conflicts of Interest

The authors declare no conflict of interest.

References

[1] S. W. Williams, F. Martina, A. C. Addison, J. Ding, G. Pardal, and P. Colegrove, "Wire + Arc Additive Manufacturing," Materials Science and Technology, vol. 32, no. 7, pp. 641-647, 2016.

[2] V. T. Le, D. S. Mai, V. T. Dang, D. M. Dinh, T. H. Cao, and V. A. Nguyen, "Optimization of Weld Parameters in Wire and Arc-Based Directed Energy Deposition of High Strength Low Alloy Steels," Advances in Technology Innovation, vol. 8, no. 1, pp. 01-11, January 2023.

[3] V. T. Le, H. Paris, and G. Mandil, "Process Planning for Combined Additive and Subtractive Manufacturing Technologies in a Remanufacturing Context," Journal of Manufacturing Systems, vol. 44, no. 1, pp. 243-254, July 2017.

[4] P. Artie Gene Jr., D. W. Gandy, G. J. Frederick, J. T. Stover, and R. Viswanathan, Method and Apparatus for Repairing Superalloy Components, U.S. Patent, 6,673,169 B1, January 04, 2004.

[5] S. Zhu, "Robotic GMAW Forming Remanufacturing Technology," Advances in Manufacturing, vol. 1, no. 1, pp. 87-90, March 2013.

[6] X. Hong, G. Xiao, Y. Zhang, and J. Zhou, "Research on Gradient Additive Remanufacturing of Ultra-Large Hot Forging Die Based on Automatic Wire Arc Additive Manufacturing Technology," The International Journal of Advanced Manufacturing Technology, vol. 116, no. 7-8, pp. 2243-2254, October 2021.

[7] Y. Li, Q. Han, I. Horváth, and G. Zhang, "Repairing Surface Defects of Metal Parts by Groove Machining and Wire + Arc Based Filling," Journal of Materials Processing Technology, vol. 274, article no. 116268, December 2019.

[8] J. H. Lee, C. M. Lee, and D. H. Kim, "Repair of Damaged Parts Using Wire Arc Additive Manufacturing in Machine Tools," Journal of Materials Research and Technology, vol. 16, pp. 13-24, January-February 2022.
[9] P. C. Priarone, G. Campatelli, A. R. Catalano, and F. Baffa, "Life-Cycle Energy and Carbon Saving Potential of Wire Arc Additive Manufacturing for the Repair of Mold Inserts," CIRP Journal of Manufacturing Science and Technology, vol. 35, pp. 943-958, November 2021.
[10] V. T. Le and H. Paris, "On the Use of Gas-Metal-Arc-Welding Additive Manufacturing for Repurposing of Low-Carbon Steel Components: Microstructures and Mechanical Properties," Welding in the World, vol. 65, no. 1, pp. 157-166, January 2021.
[11] W. Jin, C. Zhang, S. Jin, Y. Tian, D. Wellmann, and W. Liu, "Wire Arc Additive Manufacturing of Stainless Steels: A Review," Applied Sciences, vol. 10, no. 5, article no. 1563, March 2020.
[12] V. T. Le, H. Paris, and G. Mandil, "The Development of a Strategy for Direct Part Reuse Using Additive and Subtractive Manufacturing Technologies," Additive Manufacturing, vol. 22, pp. 687-699, August 2018.
[13] V. T. Le, H. Paris, and G. Mandil, "Environmental Impact Assessment of an Innovative Strategy Based on an Additive and Subtractive Manufacturing Combination," Journal of Cleaner Production, vol. 164, pp. 508-523, October 2017.
[14] A. M. King, S. C. Burgess, W. Ijomah, and C. A. McMahon, "Reducing Waste: Repair, Recondition, Remanufacture or Recycle?" Sustainable Development, vol. 14, no. 4, pp. 257-267, October 2006.
[15] X. Wang and K. Chou, "The Effects of Stress Relieving Heat Treatment on the Microstructure and Residual Stress of Inconel 718 Fabricated by Laser Metal Powder Bed Fusion Additive Manufacturing Process," Journal of Manufacturing Processes, vol. 48, pp. 154-163, December 2019.
[16] F. W. C. Farias, J. da Cruz Payão Filho, and V. H. P. M. e Oliveira, "Prediction of the Interpass Temperature of a Wire Arc Additive Manufactured Wall: FEM Simulations and Artificial Neural Network," Additive Manufacturing, vol. 48, no. A, article no. 102387, December 2021.
[17] B. Q. Chen, M. Hashemzadeh, and C. Guedes Soares, "Numerical and Experimental Studies on Temperature and Distortion Patterns in Butt-Welded Plates," The International Journal of Advanced Manufacturing Technology, vol. 72, no. 5-8, pp. 1121-1131, May 2014.
[18] J. Ding, P. Colegrove, J. Mehnen, S. Ganguly, P. M. Sequeira Almeida, F. Wang, et al., "Thermo-Mechanical Analysis of Wire and Arc Additive Layer Manufacturing Process on Large Multi-Layer Parts," Computational Materials Science, vol. 50, no. 12, pp. 3315-3322, December 2011.
[19] M. C. Bui, V. T. Le, D. X. Ta, D. S. Mai, D. M. Dinh, T. K. Doan, et al., "Thermal Analysis in Wire Arc Additively Manufactured SS308L Walls Via Numerical Simulations," Proceedings of the International Conference on Advanced Mechanical Engineering, Automation, and Sustainable Development 2021, pp. 10-15, 2022.
[20] J. C. Lippold and D. J. Kotecki, Welding Metallurgy and Weldability of Stainless Steels, Hoboken NJ: John Wiley, 2005.
[21] V. T. Le, D. S. Mai, M. C. Bui, K. Wasmer, V. A. Nguyen, D. M. Dinh, et al., "Influences of the Process Parameter and Thermal Cycles on the Quality of 308L Stainless Steel Walls Produced by Additive Manufacturing Utilizing an Arc Welding Source," Welding in the World, vol. 66, no. 8, pp. 1565-1580, August 2022.
[22] S. H. Lee, "CMT-Based Wire Arc Additive Manufacturing Using 316L Stainless Steel: Effect of Heat Accumulation on the Multi-Layer Deposits," Metals, vol. 10, no. 2, article no. 278, February 2020.
[23] R. D. Willis, F. T. Blanchard, and T. L. Conner, "Guidelines for the Application of SEM/EDX Analytical Techniques to Particulate Matter Samples," United States Environmental Protection Agency, Technical Report PB2004100988, September 2002.
[24] P. N. Bellamkonda, M. Sudersanan, and B. Visvalingam, "Characterisation of a Wire Arc Additive Manufactured 308L Stainless Steel Cylindrical Component," Materials Testing, vol. 64, no. 10, pp. 1397-1409, October 2022.
[25] V. T. Le, D. S. Mai, T. K. Doan, and H. Paris, "Wire and Arc Additive Manufacturing of 308L Stainless Steel Components: Optimization of Processing Parameters and Material Properties," Engineering Science and Technology, an International Journal, vol. 24, no. 4, pp. 1015-1026, August 2021.
[26] K. K. Singh, S. Sangal, and G. S. Murty, "Hall–Petch Behaviour of 316L Austenitic Stainless Steel at Room Temperature," Materials Science and Technology, vol. 18, no. 2, pp. 165-172, 2002.
[27] M. Kerschbaumer, G. Ernst, and P. O'Leary, "Tool Path Generation for 3D Laser Cladding Using Adaptive Slicing Technology," International Congress on Applications of Lasers & Electro-Optics, vol. 2005, article no. 604, 2005.
[28] J. Plangger, P. Schabhüttl, T. Vuherer, and N. Enzinger, "CMT Additive Manufacturing of a High Strength Steel Alloy for Application in Crane Construction," Metals, vol. 9, no. 6, article no. 650, June 2019.